



In-situ characterization of the dislocation-structure evolution in Ni micro-pillars

R. Maaß^{a,*}, M.D. Uchic^b

^a Paul Scherrer Institute, CH-5232 Villigen, Switzerland

^b Air Force Research Laboratory, Materials & Manufacturing Directorate, 2230 10th Street, Wright Patterson AFB, OH 45433, USA

Received 1 July 2011; received in revised form 2 November 2011; accepted 4 November 2011

Abstract

The high strength of micro-crystals is determined in the early flow regime, where a transition from elastic to plastic flow is obscured if compared to stress–strain data from bulk single crystals. In the present work we therefore focus on the evolution of dislocation structures in Ni micro-pillars during early deformation by employing in-situ Laue micro-diffraction. It will be shown that substantial changes in the lattice fine structure, such as multiple subgrain formation and significant rotational gradients, can be resolved prior to the onset of large strain generation. The results reveal more pronounced effects for smaller sample dimensions and also suggest that most of the evolving dislocation structure is formed prior to the occurrence of large strain bursts. A clear increase in dislocation density as a function of strain is observed, which we discuss in the context of size-dependent strain hardening and exhaustion hardening.

© 2011 Acta Materialia Inc. Published by Elsevier Ltd. All rights reserved.

Keywords: Micro-compression; Plastic deformation; Strain gradient; Single crystal; Strain hardening

1. Introduction

Micro-mechanical systems and their increasing importance demand a profound understanding of material properties at the micron or even sub-micron scale. Recent advancements in mechanical testing have enabled the systematic investigation of the effect of ever-reducing external length scales on the deformation behavior of metals [1–3]. In particular, the micro-compression test [1,4] has been employed for this purpose, where this test method consists of uniaxial compression of micron- or nano-sized pillars that are usually prepared by focused ion beam (FIB) milling. Numerous experiments on both single crystal face-centered cubic (fcc) and body-centered cubic (bcc) metals using FIB machined pillars have demonstrated a significant increase of strength as a function of decreasing sample

diameter [5–19], which for dislocated crystals seems to be prevalent irrespective of the details of the initial micro-structure [20–22]. Such experiments exhibit a stochastic plastic response, revealing the inherent intermittent nature of plastic flow [23]; an aspect that has become known after torsion experiments conducted by Tinder et al. in the mid 1970s [24], and that has been shown to be altered at small scales by the initial defect concentration [13,25].

The micro-mechanisms of size-dependent strengthening for fcc crystals remain the subject of current research, where first explanations were gleaned from theoretical considerations and simulations that emerged to: (a) a postulation that small nano-scale objects suffer from dislocation starvation [7], (b) the altering of the size distribution of dislocation sources such that the sources require a higher stress for activation, i.e. dislocation source truncation [26], and (c) a third relating to the limited number of accessible sources within small crystals, where normal dislocation interactions result in an altered strain hardening response (exhaustion hardening) within the first percent of strain [27]. In this regime the strengthening and stochastic flow can be explained with

* Corresponding author. Present address: Division of Engineering and Applied Science, California Institute of Technology, 1200 E. California Blvd., MC 309-81, Pasadena, CA 91125-8100, USA.

E-mail address: maass@caltech.edu (R. Maaß).

the activation and subsequent exhaustion of dislocations from the weakest available source. To directly verify the underlying dislocation mechanisms represents, however, an experimental challenge. At the nano-scale non-destructive in-situ TEM investigations [28–30] have provided useful insights, where for example recent results are in favor of a dislocation source-limited size-dependent yield strength [30]. Probing non-destructively the underlying micro-structural evolution at the micron scale is, however, much more delicate, but feasible with Laue micro-diffraction, as has been demonstrated for both micro-compression and micro-tension [19,31–36]. In particular, in-situ Laue diffraction experiments by Maaß et al. showed that stresses determined at strains greater than 5% are largely due to size-dependent strain hardening [34], which is compatible with the observation that the scaling exponent for the size effect in strength increases with the strain at which the stress is derived [9,37], strongly suggesting that the size-effect in flow strength at the micron scale is to a large extent due to size-dependent strain hardening, where strain hardening is understood phenomenologically without defining specific individual underlying dislocation mechanisms. Further, in-situ Laue micro-diffraction on Cu and Au micro-pillars could demonstrate dislocation storage as well as evolving lattice rotations occurring during micro-compression experiments [31,37]. Subsequently, ex-situ Laue diffraction work by Kirchlechner et al. [36] supported these findings when investigating micron-sized copper samples that had been tested in-situ in a scanning electron microscope (SEM).

In order to shed more light on the underlying evolution at different sample sizes, the present study also uses in-situ Laue micro-diffraction to characterize the change in internal dislocation microstructure during a micro-compression experiment, where Laue patterns are recorded during the compression tests [32,33]. Here Ni micro-pillars that have a uniform cross-section are characterized, so that the measured strain-hardening behavior of the sample is not an artifact of the test sample geometry. In this way the evolution of the evolving microstructure can be followed as a function of strain, elucidating the deformation processes taking place in micro-pillars. The aim of this report is to demonstrate that the Laue spot dynamics exhibit a clear signature of dislocation storage as a function of the loading

history. Further it will be shown that a substantial part of the first initial steep loading segment can contain extensive dislocation activity even though the total plastic strains during this stage are minimal; a result that is supportive of the view comprised in the protocol of exhaustion hardening [6,26,27].

2. Experimental

2.1. Investigated material

The investigated pillars were machined by focused ion beam (FIB) milling from two different single crystals that were grown from the melt with the Czochralski method. The original 100 μm thick single crystal foils were thinned by electropolishing until a $\sim 30 \mu\text{m}$ thick edge was obtained. Subsequently a set of single slip oriented ($\sim \langle 123 \rangle$) pillars was prepared on each of the thinned crystal edges by using the lathe ion milling technique [1]. An SEM image shows a set of as-prepared pillars in Fig. 1a with a view axis close to the incoming X-ray direction. Here we report on three pillars that were tested in-situ with diameters of 8 μm , 4 μm and 1 μm . The pillars had no side-wall taper and an aspect ratio of ~ 2.7 – 2.9 . The 8 μm sample was from one of the two crystals, and the 1 and 4 μm sample from the other crystal, which results in different diffraction peaks for the pillars prepared from the two different crystals because of slightly different orientations of the crystals relative to the incoming beam.

2.2. In-situ micro-compression

The micro-compression experiments were performed using a custom designed in-situ micro-compression device (MCD, lateral stiffness of $\sim 10^4 \text{ N m}^{-1}$) [32,33] that was operated in a load controlled mode with loading rates of $3 \mu\text{N s}^{-1}$ (8 μm), $1 \mu\text{N s}^{-1}$ (4 μm) and $0.3 \mu\text{N s}^{-1}$ (1 μm). A single crystal diamond flat punch tip with an end diameter of 22 μm was used as a compression anvil. During compression the sample is illuminated at the MicroXAS beamline of the Swiss Light Source in a Laue transmission geometry with a polychromatic X-ray beam containing an energy distribution from 2 to 22 keV. The X-ray beam was

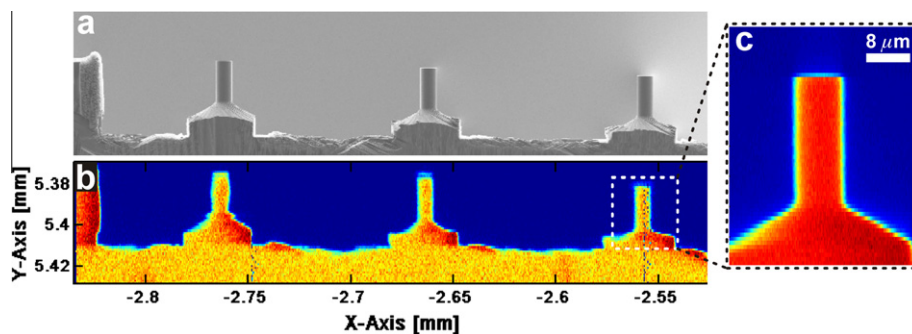


Fig. 1. (a) A SEM micrograph of three undeformed 8 μm Ni pillars. The corresponding fluorescence map is shown in (b), and a more precise fluorescence scan of one of the pillars is shown in (c).

focused with a set of Kirkpatrick–Baez mirrors, yielding a beam size of 1 μm as determined by knife edge scanning. During in-situ testing, the beam was placed on the central vertical axis and $\sim 1/3$ – $1/2$ of the pillar height below the pillar top. Note at this stage that the constant beam size leads to very different volume fractions probed during in-situ testing, which is $\sim 0.6\%$ for the 8 μm , 2.3% for the 4 μm and 36% for the 1 μm pillar. Since the in-situ Laue measurements provided information from a small region of the sample only, these dynamic measurements were complemented by acquiring two-dimensional (2-D) Laue pattern maps of the entire sample for the 8 and the 4 μm pillar both before and after the experiment. In such a way the micro-structural changes across the entire sample were obtained. Locating the micro-pillars in the micron-sized beam was done by positioning the sample in the focal plane of the beam, scanning the sample through the beam, and recording the emitted X-ray fluorescence. This way of localization produces 2-D intensity maps, of which one example of three 8 μm pillars is shown in Fig. 1b, where the same sample set as in Fig. 1a is imaged by fluorescence light, and Fig. 1c depicts a higher resolution view on a single pillar. Scattered X-rays were recorded on a 2-D Photonic Science FDI-VHR 150 charged coupled device (CCD) with a pixel size of 31 μm . The sample-to-detector distance was ~ 50 mm, which was calibrated with a single crystal reference Si wafer.

2.3. Diffraction data analysis

Recorded Laue patterns were indexed based on the triangulation method using a similar routine to what is used in Ref. [38], followed by an automated fitting procedure. During in-situ testing the diffraction peaks can exhibit the following phenomena: (a) the development of peak asymmetries, (b) collective peak movements and (c) peak splitting. Peak asymmetries are due to lattice curvatures, e.g. strain gradients, and can therefore provide information about arrangements of excess dislocations (geometrically necessary dislocations, GNDs) that lead to local lattice curvatures [39]. At the limit of a defect-free single crystalline sample the full width at half maximum (FWHM) ratio in degrees of a peak should be identical to a Si wafer reference peak, which was measured to 0.06° in both the radial detector dimension (θ) and the azimuthal dimension (ψ). A higher density of excess dislocations of one sign causes a lattice curvature that will distort the peak [40]. The peak distortion can be expressed by the magnitude ratio of the minor (ν) and major (ξ) peak axis. Changes in peak positions are a signature of lattice rotations or elastic deviatoric strain gradients [41]. Upon collective peak movements, fitting of the recorded Laue patterns as a function of strain gives access to the local lattice rotations in the illuminated volume during compression. In addition to lattice curvatures and lattice rotations, Laue patterns can exhibit peak splitting, also referred to as polygonization [41]. A sudden peak split of an asymmetric Laue peak is a signature of a

plastically bent portion of the crystal, which breaks up into smaller disoriented sub-volumes (separated by geometrically necessary dislocation boundaries, GNBs) that each diffract with slightly different angles [41,42].

3. Results

3.1. Mechanical behavior

Fig. 2a–c displays the obtained stress–strain curves of the three samples. In the case of the 8 μm and 1 μm pillar a stress–strain curve taken from Ref. [6] has been added for comparison between the in-situ tested samples and those tested ex-situ with a commercial MTS nanoindentation system. The numbers along the in-situ flow curves indicate the points at which diffraction patterns were recorded. Stress–strain curves that start at strains greater than zero have been displaced in order to facilitate comparison between the different flow curves. The 8 μm pillar was subjected to three consecutive loadings, of which the first one reached ~ 40 MPa. As micro-structural changes are most prominent throughout the latter two cycles only these two ones are shown here. With decreasing pillar size the number of diffraction patterns recorded along the stress–strain curves decreases due to a trade-off between the constant detector acquisition time, lower loading rates and dropping maximum forces. A 2-D Laue pattern map was acquired after each loading curve for the 8 and the 4 μm samples.

The displayed stress–strain curves for the three samples are qualitatively in very good agreement with the original work on Ni pillars. The 8 μm pillar has a macroscopic yield stress of ~ 110 MPa, which is also the case for the 4 μm pillar. Much higher stresses are experienced by the 1 μm pillar that macroscopically yields at close to 410 MPa, which is a tremendous increase in strength compared to a bulk yield stress of ~ 5 – 35 MPa [6,43,44]. Note that a small strain burst can be observed in the flow curve of the 1 μm sample at 27 MPa. This is very similar to one of the two curves taken from the literature [6]. As is commonly observed in micro-compression experiments, the initial slopes of the loading curves give lower elastic moduli values than are known for macroscopic single crystal testing. The low moduli measurements can usually be attributed to alignment difficulties [45]. In addition to possible alignment imperfections, the moduli obtained via in-situ testing can also be lower due to the drift of the system, which can be significant because of the long in-situ test duration (as is the case in Ref. [34]).

Fig. 2b displays two representative SEM micrographs (secondary electron contrast) of the 8 μm pillar after deformation. The image taken at a tilted view reveals some contamination on the sample top and some clearly visible slip lines that match the geometrically predicted slip plane, that is the (-111) plane. Imaged from a view direction corresponding closely to the incoming X-ray beam axis, the same (-111) slip lines are seen. Additionally two very

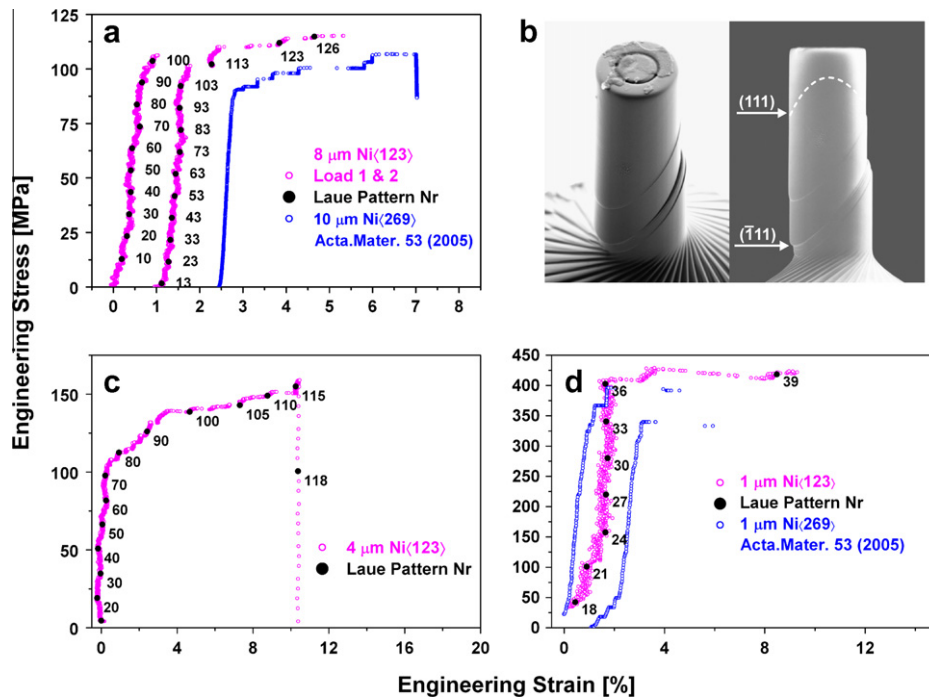


Fig. 2. Stress–strain curves of the 8 μm (a), 4 μm (c) and 1 μm (d) pillar. Both in (a) and (d) the obtained stress–strain curves are compared with curves from the original study on untapered single slip oriented Ni pillars [6]. In (b) two SEM micrographs of the deformed 8 μm pillar are shown, with indicated (-111) and (111) slip lines.

weak traces matching slip lines from the second highest Schmid factor (SF) plane, e.g., the (111) plane of which one is indicated in Fig. 2b, are distinguishable if the pillar is imaged in a detection mode that highlights surface features. Clear surface views of the 4 and 1 μm sample could not be obtained due to surface contamination observed after in-situ testing. Based on the very comparable flow behavior as compared to Ref. [6], it is assumed that plastic flow remained unaffected. In the following section, we examine in more detail the micro-plastic region of the stress–strain response, where, even though loading appears to be macroscopically elastic, the diffraction patterns exhibit changes that are related to the evolution of dislocation substructures.

3.2. Diffraction data

3.2.1. Peak shapes during initial loading

The initial Laue patterns displayed, in the case of the 8 μm pillar, the (-420) , $(-31-1)$, $(-40-2)$, $(1-11)$ and the $(1-31)$ peak, and the $(-2-22)$, $(-42-2)$, $(-24-2)$ and $(-22-2)$ peak were present in the patterns of the 4 and 1 μm pillar. Of the three highest intensity peaks [(-420) , $(-31-1)$, $(1-31)$] originating from the 8 μm pillar, the $(-31-1)$ and (-420) peaks were chosen for 2-D Pearson VII fitting as a function of accumulated Laue pattern number throughout the first and the second loading cycle of the 8 μm pillar. In the resulting plot in Fig. 3, the normalized FWHM ratios (ξ/v) are depicted for both peaks as a function of pattern number. The peak widths

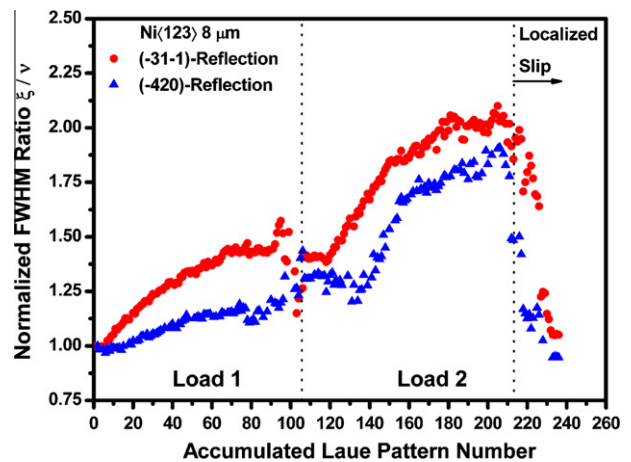


Fig. 3. The normalized $(-31-1)$ and (-420) FWHM ratio as a function of accumulated Laue pattern number for both loading cycles of the 8 μm pillar.

increase steadily to a certain point prior to the strain burst between pattern 111 and 112 (Fig. 2a, load 2). The precise moment at which the peak width reduces cannot be assigned due to scatter in the FWHM ratio, but it is clear that a build-up of excess dislocations (a strain gradient) is occurring during load 1 and most of load 2, which is released upon localized slip regaining a normalized FWHM ratio close to one. It is important to note that this Laue measurement of the reduction in peak width does not indicate that the dislocations associated with the strain gradient have glided out the micro-sample, but rather that

they are no longer within the probed volume, which in this case is as small as 0.6% of the total pillar volume. From the starting FWHM ratio of load 2 it is evident that the formed local strain gradient is a result of plastic deformation, that is, a storage of GNDs, since the fitted FWHM ratio for load 2 starts approximately at the same value where the peak width ratio ended after load 1.

As a representative reflection, the $(-2-22)$ diffraction peak from the as-prepared 4 μm pillar is shown in a truncated 2-D plot in Fig. 4a, where the color code truncation is set to 50%, thus representing the peak's FWHM in red. The x -axis reads 2θ (2θ), and the y -axis Psi (ψ), both being in degrees, which is indicated in Fig. 4b. All 2-D peak plots in Fig. 4 are displayed in the same way. The initial peak width is 0.10° in 2θ and 0.08° in ψ . After loading to 82 MPa, which is still along the macroscopically elastic loading, the $(-2-22)$ peak remains unsplit, but broadens significantly (increase in dislocation density), attaining radially $\sim 0.3^\circ$ and azimuthally $\sim 0.4^\circ$, as can be deduced from Fig. 4b. Note that both Fig. 4a and Fig. 4b are plotted with identical coordinates. Additionally the $(-2-22)$ peak (and also the other reflections not shown here in detail) has moved during the first 82 MPa loading, describing a local lattice rotation. Another peak (not shown here), namely the $(-22-2)$ reflection, forms a low intensity sub-peak along the macroscopically elastic portion of the stress–strain curve. Following further the stress–strain curve into the macroscopically plastic regime, the peaks evolve to more complex shapes exhibiting peak dynamics including peak movements, asymmetric shapes and peak splitting. Both the $(-22-2)$ and the $(-2-22)$ Laue spot are depicted at 6.7% strain in Fig. 4c (2-D angular plot)

and Fig. 4d (three-dimensional intensity profile), respectively. At that strain the $(-22-2)$ peak has recombined but is both asymmetric and strongly broadened as a result of dislocation accumulation, extending azimuthally over almost 0.6° (Fig. 4c). The $(-2-22)$ peak is split at 6.7% strain and represents thus a local polygonization process, that is, the formation of dislocation boundaries. Keep in mind that the 1 μm beam probes only $\sim 2.3\%$ of the total pillar volume. No information from the remaining volume is available during loading.

An even more complex peak dynamics occurs in the 1 μm pillar. For instance the $(-2-22)$ and $(-22-2)$ Laue spot recorded during in-situ testing reveal scattered intensities along the macroscopically elastic loading portion that are summarized for six different stresses up to ~ 400 MPa in Fig. 5. Several interesting features can be derived from the peak dynamics: (a) a double peak is present in the as-prepared condition, which could be determined to be the substrate contribution, as is indicated in Fig. 5. In fact the pillar is rotated by 0.55° relative to the underlying bulk, being similar to a 0.8 μm Au(346)-pillar reported on earlier [46]; (b) the $(-22-2)$ peak clearly moves relative to the substrate peak during the first ~ 200 MPa, being a sign of early lattice rotation; (c) from ~ 200 MPa on, the peaks unequivocally describe a crystallographic orientation distribution that attains an angular spread of $\sim 2.5^\circ$ radially and $\sim 2^\circ$ azimuthally at three-quarters of the macroscopically elastic part, as displayed in Fig. 4e and f, where the as-prepared condition (Fig. 4e) is directly compared in an angular 2-D plot to the condition prevailing at 300 MPa (Fig. 4f); (d) there is only little development of the intensity spread between the moment the break-away stress is

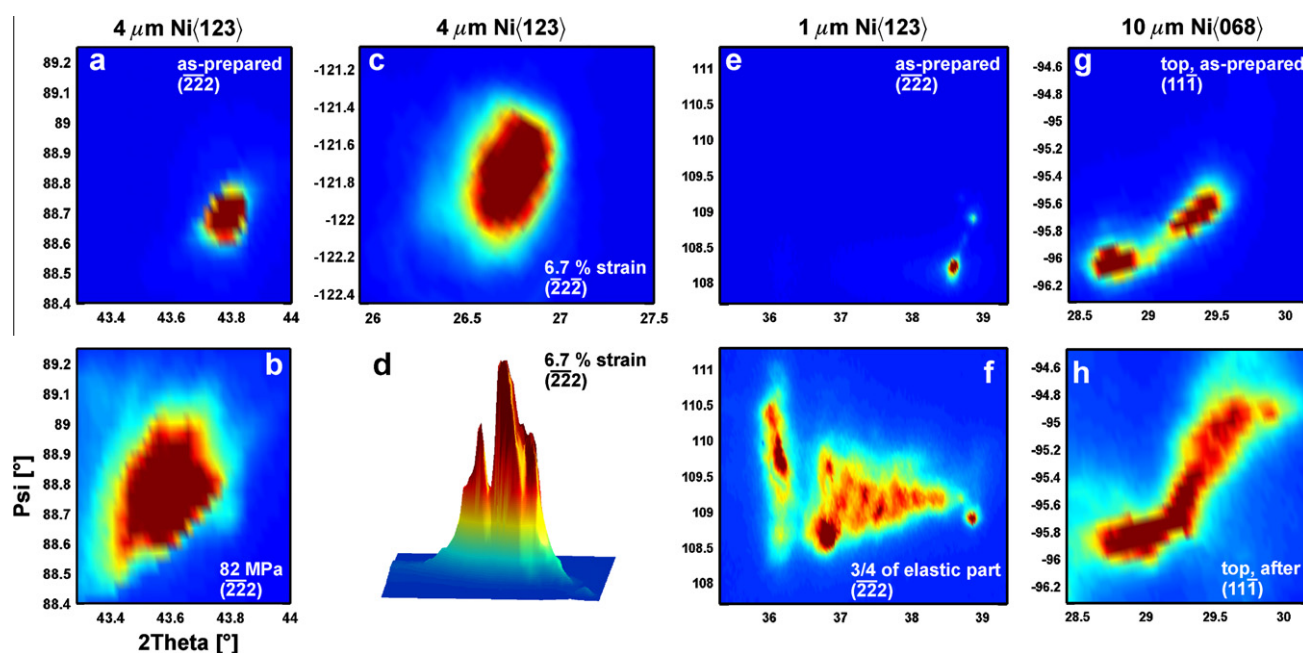


Fig. 4. (a) The initial $(-2-22)$ peak of the 4 μm pillar, (b) the same peak at 82 MPa, (c and d) the $(-22-2)$ and $(-2-22)$ peak of the 4 μm pillar at 6.7% strain, respectively, the $(-22-2)$ peak of the 1 μm pillar before loading (e) and at ~ 300 MPa (f), the $(11-1)$ peak of a 10 μm pillar from a previous study [47] at the top of the sample before loading (g) and after loading (h).

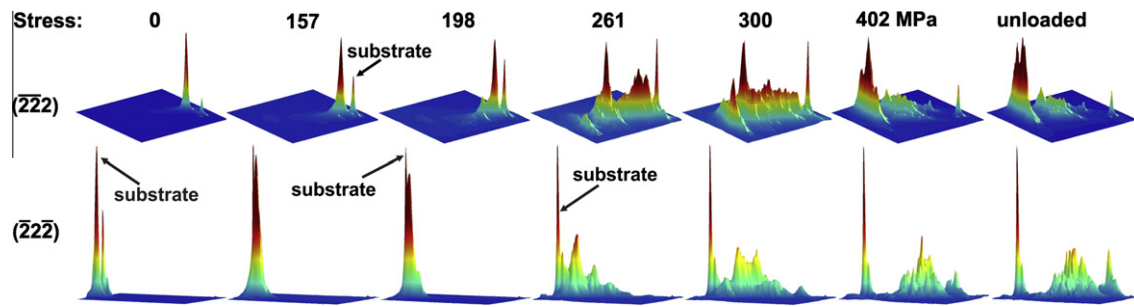


Fig. 5. Both the $(-2-22)$ and the $(-22-2)$ peak of the $1\ \mu\text{m}$ pillar shown for several stresses up to the break-away stress and for the end/unloaded condition. The substrate reflection is indicated in both cases. The peak topology of the $(-2-22)$ reflection at 300 MPa is also displayed in angular coordinates in Fig. 4f.

attained (402 MPa) and at the end of the flow curve (unloaded) after $\sim 9.3\%$ strain. Taking ~ 400 MPa as the stress at which the relationship between the engineering stress and the micro-pillar diameter is determined, the pillar is precisely matching original results on single slip oriented Ni pillars [6].

3.2.2. Spatially resolved diffraction spots

After each loading cycle 2-D Laue pattern mapping was conducted for the two larger pillars. These maps enable one to search for plastic deformation that is spatially resolved over the entire pillar. Fig. 6 shows in (a) the $(-31-1)$ map of the $8\ \mu\text{m}$ pillar after load 1 and in (b) after load 2. Fig. 6c depicts the $(-22-2)$ map of the $4\ \mu\text{m}$ sample. The scanning steps are $2\ \mu\text{m}$ in Fig. 6a and b and $1\ \mu\text{m}$ in Fig. 6c. In addition to the three maps, selected peak profiles are displayed next to each map that are labeled with numbers that link these peak images with their positions on the 2-D map. After the first load, the $8\ \mu\text{m}$ pillar shows peak splitting that is confined to the top of the pillar (positions 1–4). At position 5, which is close to the location where the in-situ beam was positioned, the peak is sharp and unsplit. These results clearly show that plastic deformation has occurred close to the platen–sample contact. Note that no measurable macroscopic strain was produced during this first loading cycle. Similar information was obtained from 2-D mapping of a $10\ \mu\text{m}$ pillar (aspect ratio $\sim 3:1$) containing a low-angle boundary that was reported on in a previous study [47]. In this prior work, Laue spots resolved for the upper $2\ \mu\text{m}$ of this $10\ \mu\text{m}$ sample revealed local crystallographic orientation spreads prior to the generation of measurable macroscopic strain after loading up to ~ 125 MPa. This is shown in Fig. 4g and h, which displays the $(11-1)$ peak recorded at the top of the sample before and after loading.

Fig. 6b shows that dislocation substructure formation has also occurred in the bottom half of the $8\ \mu\text{m}$ pillar after $\sim 4\%$ plastic strain (second loading cycle), as indicated at position 4. Fig. 6b further reveals that the position where the $8\ \mu\text{m}$ pillar was probed during in-situ testing did not exhibit any peak splitting or significant broadening after the second loading cycle.

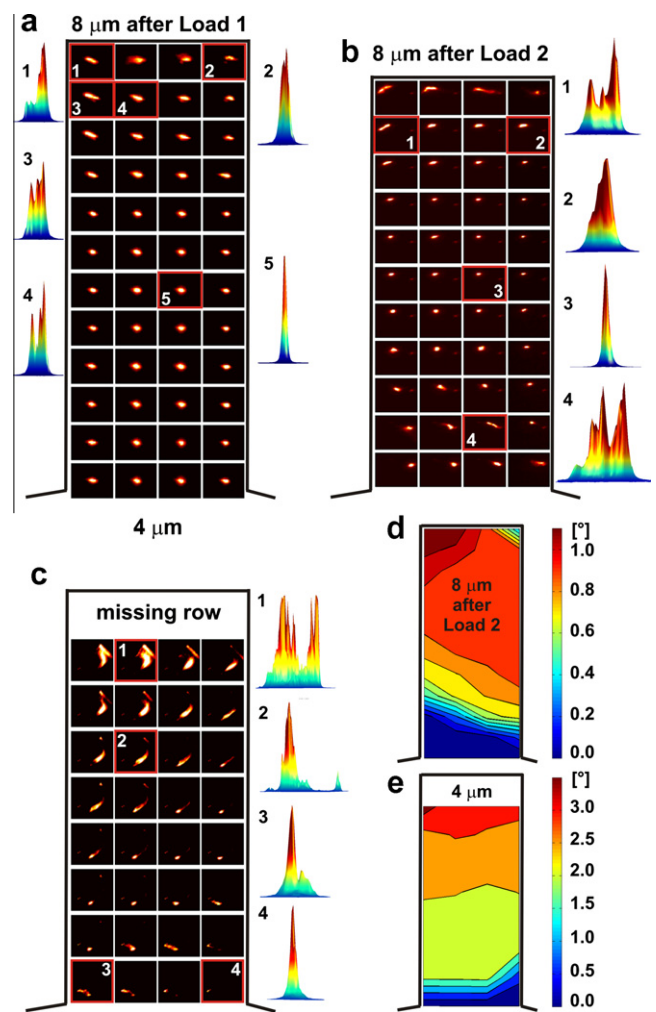


Fig. 6. A 2-D Laue spot map of the $(-31-1)$ peak from the $8\ \mu\text{m}$ pillar after load 1 (a) and after load 2 (b), where the intensity profiles are shown for selected peaks; (c) similar as in (a and b) but for the $4\ \mu\text{m}$ pillar displaying the $(-22-2)$ peak with four selected intensity profiles; (d and e) the spatially resolved CA rotation of the $8\ \mu\text{m}$ and $4\ \mu\text{m}$ pillar, respectively.

The 2-D map shown in Fig. 6c indicates the appearance of the peak topology resolved over the $4\ \mu\text{m}$ pillar, from which it is concluded that peak splitting is more pro-

nounced in the upper left corner, suggesting an asymmetric stress state during deformation. In the map of the 4 μm pillar in Fig. 6c, the upper row is missing due to an unanticipated global sample shift relative to the beam, e.g. the scan area did not cover the very top of the sample. Going from top downwards, the peak profiles 1–4 suggest a decreasingly developed dislocation substructure, where it is noteworthy that the peak profile 1 has an angular ψ spread of $\sim 3.5^\circ$. When comparing the positions of the peaks from scan step to scan step along the vertical axis in Fig. 6b and c, a peak-position shift evidencing lattice rotations is discernible, which will be presented in more detail in the following section.

3.2.3. Rotation of the compression axis

The lattice rotations qualitatively visible in Fig. 6b and c can be calculated from the change in the compression axis (CA) orientation from scan step to scan step over the 2-D maps. This has been done for both the 8 and the 4 μm pillar, as is displayed in Fig. 6d and e, where the angular offset of the CA relative to the bulk material is plotted. The spatially resolved CA rotation increases in both cases from bottom to top, providing evidence for evolving rotational gradients in the deforming pillars. In the 8 μm pillar the maximum rotation amounts to $\sim 1.2^\circ$, and to 3.5° in the 4 μm sample. Given the missing upper row of the 2-D scan, the local rotations could even be higher in the top 1 μm of the 4 μm pillar. Despite the low spatial resolution over the pillars, it is clear that the most intense lattice rotation occurs directly under the sample–indenter tip interface.

Resolving spatially the angular change of the CA via Laue pattern fitting provides additional information about the other principal laboratory axes. The angular change of the three orthogonal crystal axes (the CA, the beam axis (Z) and the mutual orthogonal X-axis) is shown in Fig. 7 as a function of pillar (8 μm) height for (a) the as-prepared state, (b) after load 1, and (c) after load 2. The angular change of the Z-axis along the pillar height in Fig. 7a is much larger than the numerical noise from the fitting rou-

tine ($\sim 10^{-4}$ for 10 fits of patterns taken at the same location on the sample) and represents thus small local crystallographic orientation variations. Furthermore, Fig. 7b shows that two axes (CA and Z) change their orientation gradually from bottom to top after being loaded once, whereas the X-axis remains at low angular offsets. This describes a rotation of the crystal coordinate system around an axis oriented closely with the X-axis ($\sim [65-7129]$). In fact the rotation axis ($\sim [78-6018]$) of the almost vertical $(-1-11)$ plane (SF close to zero) is only 11° off the crystal's X-axis but resides in the same plane.

Fig. 7b shows that a rotation did occur in the upper part of the 8 μm pillar after load 1, and that the initial orientation inhomogeneities between 7 and 17 μm reduced, compared to the as-prepared state. An inset in Fig. 7c shows the deformed 8 μm pillar imaged by SEM that is correlated with different data points taken along the pillars vertical axis after deformation. Note that the SEM inset has been slightly distorted to fit the graph's X-axis. A dashed line along the pillar indicates where the line scan during the 2-D mapping has been taken relative to the central pillar axis. This correlation demonstrates that the largest rotational gradient is present in the region of localized slip and that the pillar top experienced additional localized rotations.

Instead of resolving the rotation after each loading cycle along the vertical pillar axis, it is also possible to follow the lattice rotation in the illuminated volume during in-situ testing. This has been done for all studied samples and is displayed in Fig. 8 up to 5% strain. The fitting of the 1 μm pillar was stopped at pattern 29 (261 MPa), which means before reaching the break-away stress, due to the very complex intensity evolution of the Bragg reflections and thus increasing fitting uncertainties.

From Fig. 8 one can observe that the most significant change in lattice orientation of the illuminated volume in the 8 μm pillar occurs after 2% strain, which corresponds to X-ray data after pattern 121 (~ 110 MPa). The curve of the 8 μm pillar also shows that the first burst between

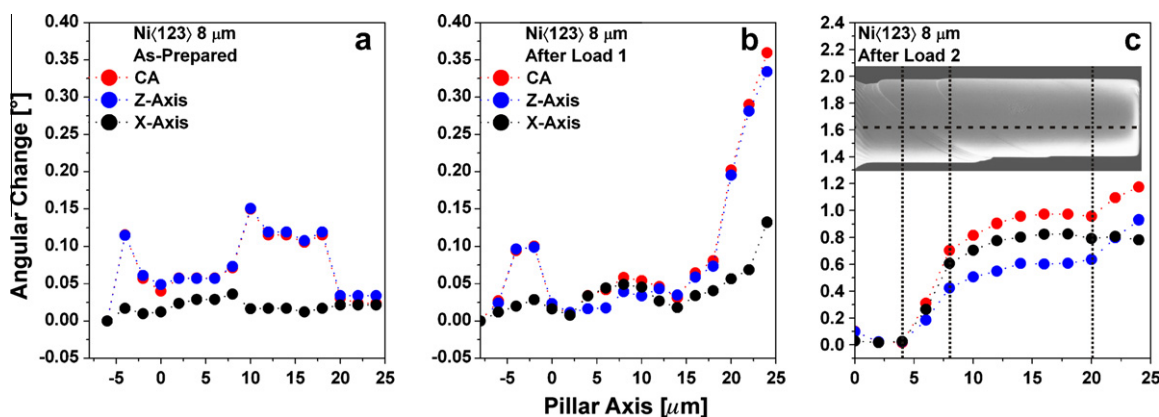


Fig. 7. The angular change of the rotating CA is shown as a function of pillar height for the 8 μm sample: (a) the as-prepared pillar, (b) after load 1, and (c) after load 2. In (c) the inset depicts the SEM micrograph of the deformed pillar being correlated with the x-axis of the graph. Note that the SEM image has been distorted slightly to match the pillar axis scale.

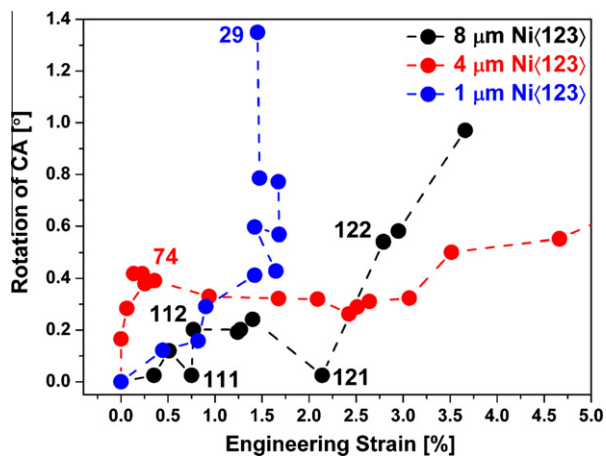


Fig. 8. The angular change of the CA as a function of the first 5% of strain for all three investigated pillars. The indicated numbers are the corresponding Laue pattern numbers.

patterns 111 and 112 (~ 101 MPa) results in $\sim 0.2^\circ$ CA rotation, after which the CA rotation decreases to close to 0° up to pattern 121, but the following strain burst between pattern 121 and 122 results in a significant increase in local lattice rotation of $\sim 0.6^\circ$.

In the probed volume of the $4 \mu\text{m}$ pillar the CA rotation behaves differently. Here the probed volume rotates already $\sim 0.4^\circ$ during the apparent elastic loading until pattern 74 (~ 104 MPa), after which macroscopic yielding takes place. Afterwards the rotation of the CA decreases slightly during the sequence of serrated flow events between 0.3 and 3% strain (see Fig. 2c). In this strain regime 6 strain bursts can be resolved, while the stress–strain curve in Fig. 2c exhibits clear strain hardening. With further increasing strain the local lattice rotation in the probed volume increases beyond 3% strain to finally reach the $\sim 2.5^\circ$ shown in Fig. 6d. At 3.7% strain, the $8 \mu\text{m}$ pillar has rotated approximately twice as much as the $4 \mu\text{m}$ pillar. Conversely, at strains exceeding 10%, the total rotation achieved in the $4 \mu\text{m}$ pillar is now 2.3° higher than in the $8 \mu\text{m}$ pillar.

The CA rotation of the small $1 \mu\text{m}$ pillar reveals increasing lattice rotations along the apparent elastic loading that is increasing much more pronounced compared to the other two pillars. During the first 100 MPa the smallest sample rotates $\sim 0.3^\circ$, which also is the case for the following 100 MPa, but afterwards a jump of $\sim 0.58^\circ$ occurs between pattern 28 (~ 241 MPa) and 29 (~ 261 MPa).

4. Discussion

4.1. Observations before the break-away stress

During the initial steep loading portion of the stress–strain curve, which also has been termed the “exhaustion hardening” regime [6,26], the Laue spot dynamics of all three samples show locally an increase in dislocation density, reflected by diffraction signatures typical for GNDs

and GNBs. For the $8 \mu\text{m}$ pillar, the in-situ measurement revealed only the development and further intensification of plastic strain gradients in the small probed volume fraction of 0.6%, but the post-loading 2-D peak mapping measurements also demonstrated that dislocation wall formation had occurred during the first loading cycle without producing any notable macroscopic strain. Despite these first plastic lattice distortions near the indenter interface, the SEM image in Fig. 2b shows that slip generating plastic strain occurred in the lower, e.g. different, part of the sample’s gauge section. The observation of peak splitting (dislocation wall formation) near the indenter head suggested compression anvil effects, which can potentially be attributed to a number of factors: lateral constraints of the test system, sample-to-platen misalignment, or local plasticity due to frictional constraints at the interface, of which aspects are for instance discussed in Refs. [34,48,49]. A similar signature was found in the upper part of a previously investigated $10 \mu\text{m}$ pillar [47], shown in Fig. 4g and h. Identifying any origin to the in Fig. 6a displayed peak splitting cannot be done with the limited data. However, the resolved rotation gradient of the CA being present after load 1 in the $8 \mu\text{m}$ pillar (Fig. 7b) is an unequivocal signature of set-up constraints that inhibit free glide on the activated slip systems. According to Fig. 7b these effects are restricted to the upper $\sim 6 \mu\text{m}$ of the $8 \mu\text{m}$ ($\sim 23 \mu\text{m}$ high) pillar, which is in agreement with the spatially resolved peaks (Fig. 6a and b).

The peaks of the smaller $4 \mu\text{m}$ pillar broaden significantly during the macroscopically elastic loading (exhaustion hardening regime) part where also first peak splitting is observed, demonstrating a clear increase in dislocation density as well as dislocation wall formation also seen for the $8 \mu\text{m}$ pillar. In addition to the observations of the strong peak broadening (e.g., increase in dislocation density) exhibited in Fig. 4a and b, it is clear from Fig. 8 that the $4 \mu\text{m}$ pillar experiences local lattice rotations of $\sim 0.4^\circ$ in the exhaustion hardening regime. Overall Fig. 8 shows for the three tested samples that the smaller the diameter, the larger is the rotation in the exhaustion hardening regime; the regime in which the strength is determined. The final rotation of $\sim 3^\circ$ determined at the end of the deformation of the $4 \mu\text{m}$ pillar suggests a moderate lateral stiffness of the testing system, if compared with data provided in Ref. [50].

The $1 \mu\text{m}$ pillar, of which a substantial part is probed during in-situ testing, provides evidence for much larger crystallographic orientation spreads than both the 4 and $8 \mu\text{m}$ sample. In fact the peak topologies depicted in Fig. 5 are similar to a signal that is obtained from a local probe of a dislocation cell structure [51,52]. This result may thus be interpreted as the development of a dislocation cell structure during the exhaustion hardening regime, which enabled the $1 \mu\text{m}$ micro-pillar to support stresses up to 400 MPa prior to break-away flow. The sub-peak formation finally spanning a crystallographic orientation spread of $2.5^\circ(2\theta)/2^\circ(\psi)$ is accompanied with rotations of

up to 1.35° when loading up to 261 MPa, indicating the activation of multiple slip systems simultaneously. Twelve sub-peaks, excluding the substrate contribution, can be distinguished in Fig. 5 at 300 MPa, which averages to an equivalent of 400 nm side length of 12 equal-sized slightly misoriented sub-volumes. Note that this estimate ignores that one peak has a clearly higher intensity, which potentially originates from either the non-linear flux-energy distribution or from a larger scattering volume than is contributed to by each of the remaining intensities.

These substructures and local crystal misorientations can consequently be seen in two different lights: firstly, they can be regarded as efficient obstacles that extend the initial elastic loading to the moment the stress is high enough that a dislocation avalanche can pass through the dislocation structure; secondly, they can be seen as a signature of the crystal's free surface, which represents the primary cause of strengthening by altering both source length distribution as well as the overall dislocation source density. Both these interpretations, however, lead to the understanding that the break-away stress is the moment at which the crystal's ability to harden has ceased to a large extent. Despite the limited amount of data, the three tested samples suggest qualitatively a higher amount of local plastic deformation (predominantly subgrain formation and lattice rotation) taking place for smaller sample sizes in the exhaustion hardening regime; a result that is based on the findings presented in Figs. 4–6 and 8. Interpreting the results with a build-up of GNDs and a crystal that contains an increasing amount of local crystal misorientations as a function of strain and decreasing size, is in agreement with recent modeling work on work hardening in micro-pillars [53]. Another pronounced difference among the three samples is the amount of CA rotation prior to the break-away stress, where an increase for decreasing sample size is observed. We acknowledge that more statistics are needed to verify this observation.

In order to quantify our obtained rotational gradients in terms of an equivalent GND density, we follow the approach used by Demir et al. [54], and calculate the density by using $\rho_{GND} = \omega/xb$, where ω is the angular rotation over the distance x , and b the Burgers vector. As an approximation we set x as being half the pillar height, which means that we interpret the angular rotation described in Fig. 8 as the highest rotational value between the pillar base and the pillar center. This is a reasonable assumption, since the rotational gradients for micro-pillars tested in similar devices follow a rather monotonic increase between pillar bottom and top [31,37,55]. Fig. 9 shows the obtained equivalent GND-density as a function of strain normalized with respect to the break-away stress defined as the strain at the recorded diffraction pattern 111 (8 μm), 74 (4 μm) and 36 (1 μm). Note that the underlying scatter in the stress–strain data in Fig. 2 also is reflected in the trends apparent in Fig. 9. The resulting GND density clearly indicates an increasing dislocation density prior to the break-away stress with decreasing pillar size.

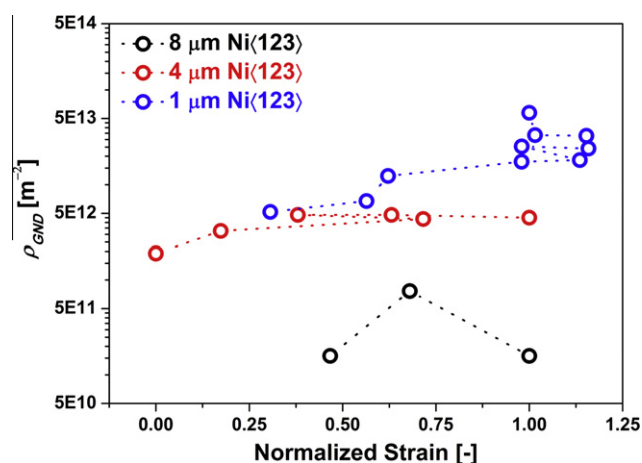


Fig. 9. The equivalent GND density as a function of normalized engineering strain (normalized to the strain at which each micro-pillar shows break-away flow). GND density calculations have been generated from the data presented in Fig. 8, omitting the data point at the origin.

Despite the clear increase in GND density in the very early part of the stress–strain curve, it has to be pointed out that a strengthening entirely based on GNDs is not sufficient to rationalize the size-effect in strength [54]. Other factors, such as the availability and strength of dislocation sources in relation to the sample size, have to be considered; all of these are beyond the experimental means of Laue micro-diffraction.

Nevertheless, the observed features provide experimental in-situ evidence for dislocation accumulation during the exhaustion hardening regime in the illuminated volume. That means that locally the lattice distorts plastically without generating substantial macroscopically resolvable strain, and thus is compatible with a scenario where GNDs arrange to accommodate imposed deformation inhomogeneities [57] until significant plastic strain is generated by mobile dislocations that move to relax the internal stress state at the break-away stress or minute discrete strain jumps occurring earlier.

4.2. Observations after the break-away stress

At higher strains the in-situ signal from the 8 μm pillar provides no evidence for dislocation substructure formation in the probed volume. However, the spatially resolved diffraction peaks taken after load 2 (Fig. 6b) exhibit qualitatively the same information as was gained from Fig. 6a, with peak splitting in the upper $\sim 4 \mu\text{m}$ of the pillar. Additionally dislocation wall formation did occur in the lower 4 μm of the pillar, as is depicted in Fig. 6b. Hence the 8 μm pillar experienced a dislocation substructure formation in both end regions of the pillar. The CA rotation progressively increases, going from pillar base to pillar top (Fig. 6d), a result very compatible with other in-situ work on Cu [31] and GaAs micro-pillars [55], and which has been attributed to different degrees of lateral testing stiffness [50]. In contrast to the formed rotational gradient within

the pillar and dislocation substructure formation, the SEM image shown in Fig. 2b presents a simple picture of slip on the predicted slip plane. From the slip lines and the stress–strain curve alone, it is reasonable to associate the pillar's plastic response to easy glide with the activation of one slip system, but the gradient of lattice rotations of over 1° and the dislocation substructure formation are rather a signature of multiple slip systems being activated. This is especially the case for the $4\ \mu\text{m}$ and the $1\ \mu\text{m}$ pillar, where these features become more pronounced. Considering the first strain burst of the $8\ \mu\text{m}$ pillar and the CA rotation (Fig. 8) of 0.2° shows that the sample is already at low strains constrained to such an extent that the system rotates once a collective dislocation event allows this.

Both the 1 and $4\ \mu\text{m}$ pillars reveal complex peak topologies or dynamics during plastic flow. Only three diffraction patterns were recorded while the $1\ \mu\text{m}$ pillar exhibited significant plastic flow up to 9.3% strain, and for this sample the signals were qualitatively not different from what was observed at the end of the exhaustion hardening regime. This indicates that the formed dislocation substructure does not change notably in density (and arrangement) in the regime of macroscopic flow, which is in agreement with TEM investigations for similar samples [56], and for in-situ TEM straining of sub-micrometer Al thin films [58]. By comparison, many diffraction patterns were recorded for the $4\ \mu\text{m}$ pillar after the break-away stress. Here the peaks exhibit complex dynamics that are typically a signature associated with a locally evolving dislocation structure, which are evidence that the flow regime of micro-pillars cannot be viewed as a highly idealized process of a succession of elastic loadings followed by strain bursts in which the mobile dislocations run out of the crystal. Thus, the emerging picture at the micron-scale describes a deformation process in which the density of dislocations increases instead of attaining a dislocation starved state, which is distinctly different from, but also compatible with, the dislocation starvation model that is sought to dominate in the nanometer regime [59], where image forces and the scarcity of pre-existing dislocations may considerably gain importance. In fact, the recorded diffraction signal is a distinct signature of dislocation accumulation, dislocations collapsing into boundaries and local gradient dynamics, of which strain gradients recently have been incorporated into a one-dimensional model by Aifantis and co-workers, successfully describing and predicting flow of micro-pillars [60]. The observed differences in the scattered X-ray intensities between the three samples suggest a higher complexity and density of the forming dislocation structure with smaller sample size, a fact that again underlines the earlier expressed view that the size-effect in micro-pillars is due to a size-dependent strain hardening.

The present findings are qualitatively in agreement with TEM studies on very similar pillars showing an increase in dislocation density with decreasing pillar diameter of deformed samples [56], and is, in the case of the $1\ \mu\text{m}$ pillar,

the first experimental in-situ evidence for the suggestion that most of the dislocation structures form during the exhaustion-hardening regime [56]. Due to the small probed volume fraction during in-situ testing for the 8 and $4\ \mu\text{m}$ pillars, the here recorded data does not allow quantifying if the majority of the dislocation structure is formed during exhaustion hardening or after the break-away stress. We acknowledge that additional studies are needed to gather a more statistically representative sampling of the plastic processes in the pillars.

5. Summary

In-situ Laue diffraction was performed on single slip oriented pure Ni micro-pillars with a uniform cross-section. The experiments enabled characterization of the heterogeneous nature of plasticity and the accompanied dislocation accumulation in the micro-pillars during uniaxial compression testing. From these experiments, the following observations were made:

- Laue spots recorded during the exhaustion hardening portion of the stress–strain curve reveal evolving plastic strain gradients, peak broadening, lattice rotations and local dislocation substructure formation, where the details of the observed evolution of the Laue pattern varied from sample to sample. All these Laue spots feature evidence dislocation storage in the tested samples. The volume portions probed during in-situ testing are small for the two larger pillars, but from the data recorded for the $1\ \mu\text{m}$ pillar representing a major fraction of the total pillar volume, it is clear that most of the formed dislocation substructure for this sample is generated during the exhaustion hardening regime prior to the break-away stress.
- For the three tested pillars, increasing lattice rotations with decreasing sample diameter are observed prior to the stress at which the samples exhibit break-away flow. Converting the lattice rotations to an equivalent GND density yields an increasing dislocation density with decreasing sample size with values of the order of 5×10^{11} to $5 \times 10^{13}\ \text{m}^{-2}$ depending on sample size.
- 2-D spatial Laue pattern mapping after loading demonstrates that rotational gradients develop between the pillar base and pillar top (8 and $4\ \mu\text{m}$ pillar), and that dislocation wall formation takes place first close to the tip–sample interface ($8\ \mu\text{m}$ pillar), being a signature of imperfect mechanical testing conditions as well as contact constraints.
- The observed diffraction peak dynamics are in qualitative agreement with the reported increasing dislocation density as the diameter decreases [56], and the data provide the first in-situ experimental evidence of the evolution of the dislocation substructures that form in the exhaustion-hardening regime in micro-pillars.

The combined results provide a picture that demonstrates that plasticity in micro-pillars involves an increasing dislocation density and the formation of dislocation substructures as a function of loading history/strain, which again indicates that the size-effected flow strength at the micro-scale is, at least partly, due to a size-affected strain hardening.

Acknowledgements

R.M. gratefully acknowledges the splendid support of the MicroXAS beamline crew at the Swiss Light Source: D. Grolimund, C. Borca, and M. Willmann. Thanks go also to the Materials Science and Simulation group at the Paul Scherrer Institute: H. Van Swygenhoven, S. Van Petegem, J. Zimmermann, Stefan Brandstetter and Christian Brandl. Further, R.M. would like to acknowledge the support of Hysitron Inc. for technical support of the MCD-development. Gratitude is expressed towards P.M. Derlet and C.P. Frick for valuable discussions. R.M. also thanks the Alexander von Humboldt foundation for financial support at his current affiliation.

References

- [1] Uchic MD, Dimiduk DA. *Mater Sci Eng A* 2005;400:268.
- [2] Motz C, Schoberl T, Pippan R. *Acta Mater* 2005;53:4269.
- [3] Kiener D, Grosinger W, Dehm G, Pippan R. *Acta Mater* 2008;56:580.
- [4] Uchic MD, Dimiduk DM, Florando JF, Nix WD. *Mater Res Soc Symp Proc* 2003;753:27.
- [5] Uchic MD, Dimiduk DM, Florando JN, Nix WD. *Science* 2004;305:986.
- [6] Dimiduk DM, Uchic MD, Parthasarathy TA. *Acta Mater* 2005;53:4065.
- [7] Greer JR, Nix WD. *Phys Rev B* 2006;73:245410.
- [8] Greer JR, Weinberger CR, Cai W. *Mater Sci Eng A* 2008;493:21.
- [9] Frick CP, Clark BG, Orso S, Schneider AS, Arzt E. *Mater Sci Eng A* 2008;489:319.
- [10] Volkert CA, Lilleodden ET. *Phil Mag* 2006;86:5567.
- [11] Frick CP, Orso S, Arzt E. *Acta Mater* 2007;55:3845.
- [12] Ng KS, Ngan AHW. *Acta Mater* 2008;56:1712.
- [13] Bei H, Shim S, Pharr GM, George EP. *Acta Mater* 2008;56:4762.
- [14] Kiener D, Motz C, Schoberl T, Jenko M, Dehm G. *Adv Eng Mater* 2006;8:1119.
- [15] Greer JR, Oliver WC, Nix WD. *Acta Mater* 2005;53:1821.
- [16] Schneider AS, Frick CP, Clark BG, Gruber PA, Arzt E. *Mater Sci Eng A* 2011;528:1540.
- [17] Schneider AS, Clark BG, Frick CP, Gruber PA, Arzt E. *Mater Sci Eng A* 2009;508:241.
- [18] Lilleodden E. *Scripta Mater* 2010;62:532.
- [19] Frick CP, Clark BG, Schneider AS, Maass R, Petegem SV, Swygenhoven HV. *Scripta Mater* 2010;62:492.
- [20] Buzzi S, Dietiker M, Kunze K, Spolenak R, Löffler JF. *Phil Mag* 2009;89:869.
- [21] Jennings AT, Burek MJ, Greer JR. *Phys Rev Lett* 2010;104:135503.
- [22] Dietiker M, Buzzi S, Pigozzi G, Löffler JF, Spolenak R. *Acta Mater* 2011;59:2180.
- [23] Dimiduk DM, Woodward C, LeSar R, Uchic MD. *Science* 2006;312:1188.
- [24] Tinder RF, Trzil JP. *Acta Metall* 1973;21:975.
- [25] Phani PS, Johanns KE, Duscher G, Gali A, George EP, Pharr GM. *Acta Mater* 2011;59:2172.
- [26] Parthasarathy TA, Rao SI, Dimiduk DM, Uchic MD, Trinkle DR. *Scripta Mater* 2007;56:313.
- [27] Rao SI, Dimiduk DM, Parthasarathy TA, Uchic MD, Tang M, Woodward C. *Acta Mater* 2008;56:3245.
- [28] Shan ZW, Mishra RK, Asif SAS, Warren OL, Minor AM. *Nat Mater* 2008;7:115.
- [29] Ye J, Mishra RK, Minor AM. *Scripta Mater* 2008;59:951.
- [30] Kiener D, Minor AM. *Acta Mater* 2011;59:1328.
- [31] Maass R, Van Petegem S, Grolimund D, Van Swygenhoven H, Kiener D, Dehm G. *Appl Phys Lett* 2008;92:071905.
- [32] Maass R, Van Petegem S, Van Swygenhoven H, Derlet PM, Volkert CA, Grolimund D. *Phys Rev Lett* 2007;99:145505.
- [33] Maass R, Van Petegem S, Borca CN, Van Swygenhoven H. *Mater Sci Eng A* 2009;524:40.
- [34] Maass R, Van Petegem S, Ma D, Zimmermann J, Grolimund D, Roters F, et al. *Acta Mater* 2009;57:5996.
- [35] Bei H, Barabash RI, Ice GE, Liu W, Tischler J, George EP. *Appl Phys Lett* 2008;93:071904.
- [36] Kirchlechner C, Kiener D, Motz C, Labat S, Vaxelaire N, Perroud O, et al. *Phil Mag* 2011;91:1256.
- [37] Maass R. PhD thesis nr. 4468. Ecole Polytechnique Fédérale de Lausanne; 2009.
- [38] Tamura N, MacDowell AA, Spolenak R, Valek BC, Bravman JC, Brown WL, et al. *J Synchrotron Radiat* 2003;10:137.
- [39] Barabash R, Ice GE, Larson BC, Pharr GM, Chung KS, Yang W. *Appl Phys Lett* 2001;79:749.
- [40] Barabash RI, Ice GE, Pang JWL. *Mater Sci Eng A* 2005;400:125.
- [41] Ice GE, Barabash RI. *Dislocat Solids* 2007;13:79.
- [42] Cullity BD, Stock SR. *Elements of X-ray diffraction*. Englewood Cliffs (NJ): Prentice Hall; 2001.
- [43] Kronmüller H. *Das Magnetische Z Phy* 1959;154:574.
- [44] Frankel GS, Latanision RM. *Scripta Metall* 1986;20:681.
- [45] Zhang H, Schuster BE, Wei Q, Ramesh KT. *Scripta Mater* 2006;54:181.
- [46] Maass R, Van Petegem S, Zimmermann J, Borca CN, Van Swygenhoven H. *Scripta Mater* 2008;59:471.
- [47] Maass R, Van Petegem S, Grolimund D, Van Swygenhoven H, Uchic MD. *Appl Phys Lett* 2007;91:131909.
- [48] Kiener D, Motz C, Dehm G. *Mater Sci Eng A* 2009;505:79.
- [49] Raabe D, Ma D, Roters F. *Acta Mater* 2007;55:4567.
- [50] Shade PA, Wheeler R, Choi YS, Uchic MD, Dimiduk DM, Fraser HL. *Acta Mater* 2009;57:4580.
- [51] Levine LE, Larson BC, Yang W, Kassner ME, Tischler JZ, Delos-Reyes MA, et al. *Nat Mater* 2006;5:619.
- [52] Levine LE, Larson BC, Tischler J, Geantil ME, Kassner ME, Liu W, et al. *Z Kristallogr* 2008;Suppl.:55.
- [53] Kiener D, Guruprasad PJ, Keralavarma SM, Dehm G, Benzerga AA. *Acta Mater* 2011;59:3825.
- [54] Demir E, Raabe D, Roters F. *Acta Mater* 2010;58:1876.
- [55] Maeder X, Mook WM, Niederberger C, Michler J. *Phil Mag* 2011;91:1097.
- [56] Norfleet DM, Dimiduk DM, Polasik SJ, Uchic MD, Mills MJ. *Acta Mater* 2008;56:2988.
- [57] Gao HJ, Huang YG. *Scripta Mater* 2003;48:113.
- [58] Oh SH, Legros M, Kiener D, Dehm G. *Nat Mater* 2009;8:95.
- [59] Greer JR, De Hosson JTM. *Prog Mater Sci* 2011;56:654.
- [60] Zhang X, Aifantis KE. *Mater Sci Eng A* 2011;528:5036.